Check for updates

High Power Laser Science and Engineering, (2026), Vol. 14, e7, 8 pages.
doi:10.1017/hpl.2025.10093

HIGH POWER LASER SCIENCE AND ENGINEERING

RESEARCH ARTICLE

Efficient generation of a 100 nC electron beam via self-mode transition from LWFA to PWFA

Huitong Zhai[1,2,†], Mingyang Zhu[1,2,†], Xichen Hu[1,2,†], Jie Feng[1,2], Yifei Li[3], Bingzhan Shi[1,2], Hui Zeng[1,2], Jinguang Wang[3], Xin Lu[3,4,5], and Liming Chen[1,2]

[1]*State Key Laboratory of Dark Matter Physics, Key Laboratory for Laser Plasmas (MoE), School of Physics and Astronomy, Shanghai Jiao Tong University, Shanghai, China*

[2]*IFSA Collaborative Innovation Center, Shanghai Jiao Tong University, Shanghai, China*

[3]*Beijing National Laboratory for Condensed Matter Physics, Institute of Physics, Chinese Academy of Sciences, Beijing, China*

[4]*School of Physical Sciences, University of Chinese Academy of Sciences, Beijing, China*

[5]*Songshan Lake Materials Laboratory, Dongguan, China*

(Received 29 June 2025; revised 7 October 2025; accepted 11 November 2025)

Abstract

Laser-driven plasma wakefield acceleration (LWFA) offers exceptionally high acceleration gradients and can produce high-brightness electron beams. However, the laser-to-electron energy conversion efficiency typically remains limited to a few percent. Theoretically, the self-mode transition from LWFA to beam-driven plasma wakefield acceleration (PWFA) provides a pathway for fully utilizing the laser energy. Here, we demonstrate the single-stage LPWFA (hybrid LWFA–PWFA) scheme, validated through comparative experiments using a 300 TW tightly focused laser interacting with sub-critical density nitrogen gas targets. The experiments produce an electron beam with charge of approximately 31 nC above 6 MeV and approximately 116 nC above 2 MeV. The laser-to-electron energy conversion efficiency is approximately 6.1% (>6 MeV) and 16.4% (>2 MeV), respectively. Particle-in-cell simulations confirm that the single-stage LPWFA mechanism depletes the laser energy and enables continual electron injection. This high-charge, multi-MeV electron beam has great value in the generation of high-brightness γ-rays and high-flux neutron sources.

Keywords: energy conversion efficiency; high-charge electron beam; self-mode transition; laser-driven plasma wakefield acceleration; beam-driven plasma wakefield acceleration

1. Introduction

Laser-driven plasma wakefield acceleration (LWFA)[1] and beam-driven plasma wakefield acceleration (PWFA)[2] are both promising high-gradient acceleration schemes that address the critical limitations of traditional radio-frequency accelerators. In LWFA, an ultra-intense relativistic laser pulse drives large-amplitude plasma waves via its ponderomotive force as it propagates through a low-density plasma. In contrast, PWFA relies on the Coulomb field of a relativistic intense electron beam to excite similar plasma wakefields. In both schemes, these wakefields can trap and accelerate electrons with extremely high gradients. Despite their analogous physical principles, LWFA and PWFA possess distinct characteristics and offer complementary advantages[3–5]. LWFA can generate high-energy electron beams, yet its acceleration length is constrained by laser diffraction and dephasing length[6,7]. Conversely, PWFA circumvents dephasing limitations, but requires costly kilometer-scale traditional accelerator to deliver the high-energy, high-current electron beam needed as a driver. The hybrid LWFA–PWFA mechanism (LPWFA) bridges these limitations by employing an LWFA-derived electron beam with kA-scale current to drive the PWFA stage, synergizing the compactness of LWFA with the dephasing-free nature of PWFA.

Correspondence to: J. Feng and L. Chen, School of Physics and Astronomy, Shanghai Jiao Tong University, Shanghai 200240, China. Emails: fengjie93@sjtu.edu.cn (J. Feng), lmchen@sjtu.edu.cn (L. Chen); Y. Li, Beijing National Laboratory for Condensed Matter Physics, Institute of Physics, Chinese Academy of Sciences, Beijing 100190, China. Email: yflx@iphy.ac.cn

[†]These authors contributed equally to this work.

© The Author(s), 2026. Published by Cambridge University Press in association with Chinese Laser Press. This is an Open Access article, distributed under the terms of the Creative Commons Attribution licence (https://creativecommons.org/licenses/by/4.0), which permits unrestricted re-use, distribution and reproduction, provided the original article is properly cited.

https://doi.org/10.1017/hpl.2025.10093 Published online by Cambridge University Press

A clear separation of the LWFA and PWFA regimes can be achieved by employing dual consecutive gas jets to create two separate LWFA and PWFA stages. A steel foil or blocker tape[8–10] is typically positioned between the two gas targets to block the remaining laser energy, allowing only the electron beams to enter the second stage and exclusively drive the plasma wakefield. Over the past decade, this dual-target configuration has established LPWFA as a promising platform for transforming beam energy and brightness[3,8–13]. This approach relies on high-current LWFA-generated electron beams to drive the subsequent PWFA stage, and enables unique electron injection methods[3–5,9] in this PWFA stage. Although the conversion efficiency from integrated PWFA driver electron beam energy to integrated injected electron beam energy has already reached the record level of approximately 10% in proof-of-concept experiments[9], the overall laser-to-electron conversion efficiency is sacrificed in order to realize electron energy and brightness transformers.

The self-mode transition from LWFA to PWFA enables more complete utilization of laser energy[14] in single-stage operation[15–20]. Once the driving laser pulse is depleted in the plasma, the LWFA-accelerated electron beam autonomously acts as the main driver of the PWFA. This transition has been experimentally demonstrated under low-density conditions as a feasible method to achieve electron beam energy boosting[15–17] in the bubble acceleration regime. Recently, the numerical simulations by Horný *et al.*[18] showed that ultrashort laser pulses can generate multi-nC electron beams with energies of hundreds of MeV in the pump-depletion-dominated bubble regime. They found that the single-stage LPWFA can enable the complete depletion of laser energy within the wakefield, and 50% of the laser energy can transfer to the relativistic electrons. However, the ability of the single-stage LPWFA to achieve high laser-to-electron energy conversion efficiency has not yet been experimentally demonstrated.

In this work, we demonstrate the single-target LPWFA scheme using a 300 TW tightly focused laser interacting with a sub-critical density nitrogen gas target. By comparing top-view images and electron energy spectra obtained from 0.3 and 2 mm diameter gas nozzles, the onset hybrid acceleration in the long-nozzle configuration is identified and generates 100-nC-class multi-MeV electron beams with high laser-to-electron energy conversion efficiency. To further figure out the mechanism behind this improved efficiency, we perform quasi-three-dimensional (3D) particle-in-cell (PIC) simulations using parameters closely matched to the experiment. The simulations capture the evolution of the hybrid acceleration process, supporting single-stage LPWFA as a viable approach for producing high-efficiency, high-charge electron beams.

2. Experimental setup

The experiment was conducted using the SECUF-PW laser facility, a Ti:sapphire laser system at the ultrafast X-ray dynamics experimental station of the Synergetic Extreme Condition User Facility (SECUF), Institute of Physics, Chinese Academy of Sciences. The experimental setup is illustrated in Figure 1. A laser pulse with a central wavelength of 800 nm, full width at half maximum (FWHM) duration of 25 fs and energy of 9 J was focused onto the gas target by using an $f/4.4$ off-axis parabolic mirror. The laser pulse was focused to a spot with radius $w_0 \approx 4.7$ μm, containing approximately 47% of the total pulse energy, yielding a peak intensity of approximately 5.2×10^{20} W/cm^2 and the normalized vector potential $a_0 \approx 15.6$. Two types of gas nozzles were connected to a fast-operating valve respectively in the experiment. The first was a convergent–divergent Laval nozzle with an exit diameter of 300 μm, while the second featured a 2 mm diameter (see Appendix A). Pure nitrogen was used as the working gas to exploit ionization-induced injection and thereby enhance the electron injection rate. Offline density measurements revealed the nitrogen density profile. The 2 mm nozzle consists of a 1000 μm density up-ramp, followed by an 800 μm plateau and then a 1200 μm density down-ramp, while the 0.3 mm nozzle yielded a Gaussian-like density distribution. Plasma density was varied by adjusting the gas backing pressure. The electron spectrometer consists of an 8 cm × 8 cm permanent magnet with a maximum magnetic field of 0.98 T. The accelerated electrons were deflected by the magnet onto the phosphor screen, coupled with a 16-bit visible charge-coupled device (CCD) camera. The spectrometer covered an energy range from 7.5 to 77.5 MeV. A top-view imaging system was used to monitor the plasma channel via the scattered light. The electron beam charge was measured using 20 cm × 20 cm absolutely calibrated image plates[21–23] (IPs, Fuji Film SR series) positioned 24.5 cm away from the target along the beam axis inside the chamber. A series of energy cut-off filters allowed charge measurements across a range of energy thresholds, from more than 0.6 MeV up to more than 6 MeV.

3. Experimental results

The single-shot electron energy distributions obtained by using the 0.3-mm-diameter nozzle (shot #1) and the 2-mm-diameter nozzle (shots #2–#4) are presented in Figure 2(a). For both nozzles, the laser was focused 300 μm upstream of the nozzle center. For the 0.3 mm nozzle, the electron energy spectrum exhibits a two-temperature distribution of the form $N_e \propto e^{\frac{E}{T_{e1}}} + e^{\frac{E}{T_{e2}}}$ where $T_{e1} = 7.3$ MeV and $T_{e2} = 19.9$ MeV (Figure 2(b)), a typical signature of LWFA in high-density

https://doi.org/10.1017/hpl.2025.10093 Published online by Cambridge University Press

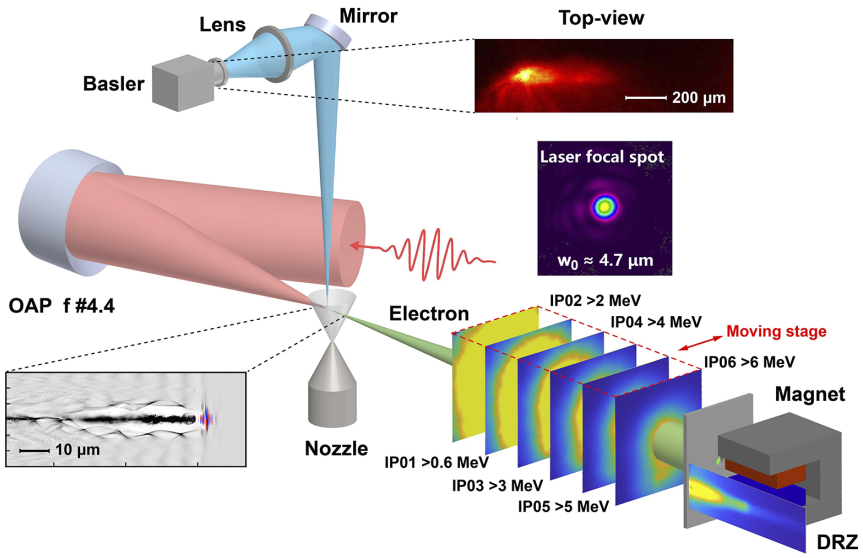


Figure 1. Schematic of the experimental setup.

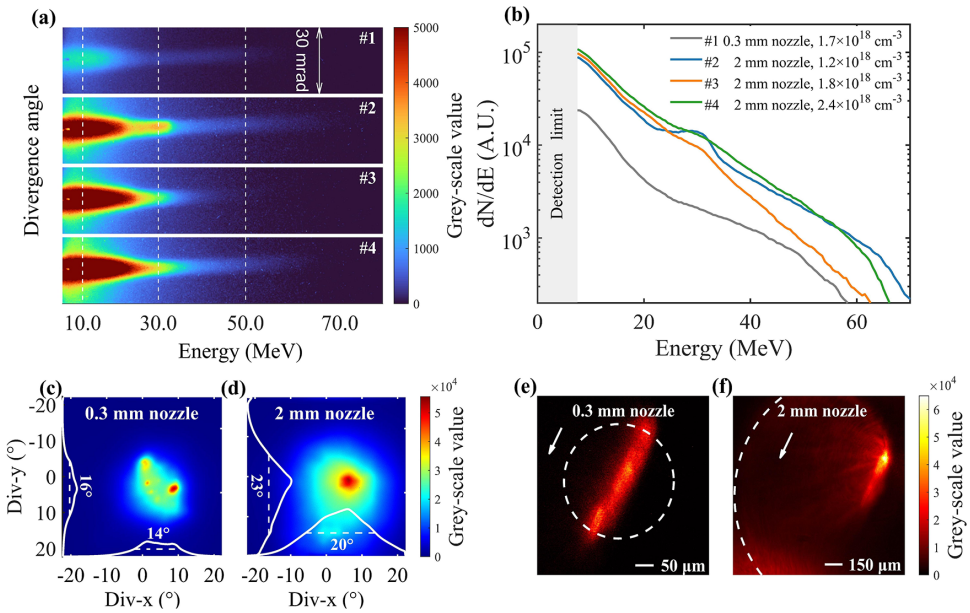


Figure 2. Experiment results of plasma wakefield acceleration. (a) Representative single-shot electron energy distributions for the 0.3-mm-diameter nozzle (shot #1) and the 2-mm-diameter nozzle (shots #2–#4) at different nitrogen densities: shot #1 (1.7×10^{18} cm^{-3}), shot #2 (1.2×10^{18} cm^{-3}), shot #3 (1.8×10^{18} cm^{-3}), shot #4 (2.4×10^{18} cm^{-3}). (b) Corresponding electron energy spectra for shots #1–#4. (c), (d) Angular distribution of electron beams for the 0.3 and 2 mm nozzles, respectively. (e), (f) Top-view images of side Thomson-scattered light for the 0.3 and 2 mm nozzles, respectively. White dashed lines indicate nozzle boundaries, while white solid arrows denote laser propagation directions.

plasma conditions[24]. The measured electron beam charge above 6 MeV was 7.3 nC, with an FWHM divergence angle of approximately 15° at a nitrogen density of approximately 1.7×10^{18} cm^{-3} (Figure 2(c)), and the laser-to-electron energy conversion efficiency was approximately 1.4%. In contrast, the energy spectra obtained from the 2 mm nozzle show significant enhancements within the nitrogen density range from 1.2×10^{18} to 2.4×10^{18} cm^{-3} (Figure 2(b)). Notably, at a density of 1.2×10^{18} cm^{-3}, a prominent plateau emerges around 30 MeV. The integrated charges above 6, 4 and 2 MeV are 31, 63 and 116 nC, respectively, significantly exceeding the prediction from the nonlinear bubble regime scaling law[6,25] (see Appendix B). The electron spectrum for energies below 7.5 MeV was extrapolated by fitting the measured charges across different energy thresholds. The laser-to-electron energy conversion efficiency reaches 6.1%, 10.7% and 16.4% for electron energy above 6, 4 and 2 MeV, respectively (see Appendix C). Here, the energy conversion efficiency is defined as the ratio of the total kinetic energy of accelerated electrons to the incident laser energy. The

https://doi.org/10.1017/hpl.2025.10093 Published online by Cambridge University Press

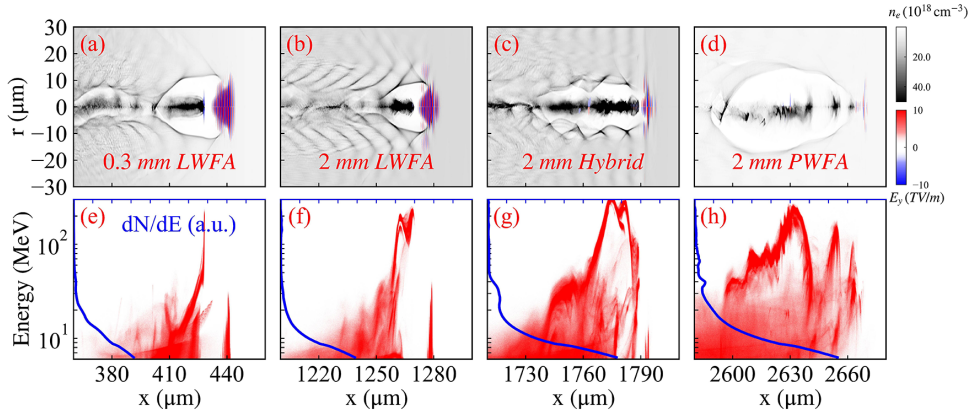


Figure 3. Simulation results of plasma wakefield acceleration. (a)–(d) Simulated snapshots of the electron density distribution and transverse electric field. (e)–(h) The corresponding longitudinal phase space of the electron beam and electron energy spectrum above 6 MeV.

divergence of the electron beam was approximately 22° (Figure 2(d)).

The top-view imaging of scattered light was used to estimate the laser propagation distance, offering insights into the physical mechanisms behind the spectral enhancement. The laser propagation direction is indicated by white arrows in Figures 2(e) and 2(f). For the 0.3 mm nozzle, the laser propagates entirely through the gas target (Figure 2(e)). In contrast, for the 2 mm nozzle, the scattered light extends only half of the nozzle length (Figure 2(f)). This suggests that in the longer nozzle, a transition to PWFA may occur after significant laser energy depletion. In addition, we rotated the magnetic spectrometer to deflect electrons in the plane perpendicular to the laser polarization to assess the presence of direct laser acceleration (DLA). If DLA mechanisms were present, electrons would gain preferential momentum along the laser polarization. The spectrum would split into a forked structure at the high-energy tail[26,27]. However, no forked structure was observed in our spectrum, confirming that the contributions from DLA are negligible.

4. Simulation results

To investigate the physical mechanism behind the enhanced electron beam conversion efficiency, we performed simulations using the quasi-3D PIC code FBPIC[28]. The simulation parameters were set to closely match the experimental conditions. A linearly polarized laser pulse along the x-axis with wavelength of 800 nm, laser intensity $a_0 = 14$, pulse duration of $\tau_0 = 25$ fs (FWHM) and spot size of $w_0 = 4.72$ μm was focused into a pure nitrogen plasma. For the 2 mm nozzle, the plasma density profile consisted of a 1000 μm up-ramp, an 800 μm density plateau and a 1200 μm down-ramp. In comparison, the 0.3 mm nozzle provided a Gaussian density profile with an FWHM of 300 μm and a total length of 600 μm. The simulations were performed in a cylindrical geometry using two azimuthal modes. The simulation window size was 160 μm (longitudinal, x) × 60 μm (radial, r), with grid resolutions of $\Delta x = \lambda/20$ and $\Delta r = \lambda/4$, respectively.

Figure 3 presents the evolution of the electron density distribution, transverse electric field, phase space (x, E_k) of the electron beam and electron energy spectrum above 6 MeV for two distinct nozzles. The nitrogen plasma densities were set to 1.7×10^{18} cm^{-3} for the 0.3 mm nozzle and 1.2×10^{18} cm^{-3} for the 2 mm nozzle. For the 0.3 mm nozzle, the laser ponderomotive force rapidly expels electrons to form an ion cavity structure, also known as plasma bubble (Figures 3(a) and 3(e)). This structure captures and accelerates electrons, generating an electron beam of approximately 6 nC, in agreement with experimental measurements. For the 2 mm nozzle, the acceleration process evolves through three distinct stages, namely LWFA, LWFA–PWFA hybrid and PWFA. In Figures 3(b) and 3(f), the early stage is dominated by LWFA, accompanied by minor contributions from ponderomotive acceleration and DLA[29,30]. In the hybrid LWFA–PWFA stage (Figures 3(c) and 3(g)), the wakefield is co-driven by both the laser and the electron beam, which can be described by $\left(\frac{\partial^2}{\partial t^2} + {\omega_p}^2\right)\frac{\delta n}{n_0} = -{\omega_p}^2\frac{n_b}{n_0} + c^2\Delta\frac{\vec{a}}{2}$[31]. Here, ω_p denotes the plasma frequency, n_b is the electron beam density and $\delta n = n_e - n_0$ represents the plasma density perturbation, where n_e and n_0 are the local and background plasma densities, respectively. As the laser is gradually depleted, the electrons accelerated by the laser cease gaining energy and instead begin to drive the plasma wakefield, which in turn accelerates the tail of the electron beam. At this point, the laser pulse energy is nearly fully depleted in the plasma, and the laser-to-electron energy conversion efficiency reaches its maximum. In the pure PWFA stage, as shown in Figures 3(d) and 3(h), a small fraction of the high-energy drive beam transfers its energy to multiple low-energy witness beams, leading to a significant increase in the charge of the low-energy electrons. In this case, the electron charge above 6 MeV is approximately 26 nC, which is consistent with the charge levels in the experiment.

https://doi.org/10.1017/hpl.2025.10093 Published online by Cambridge University Press

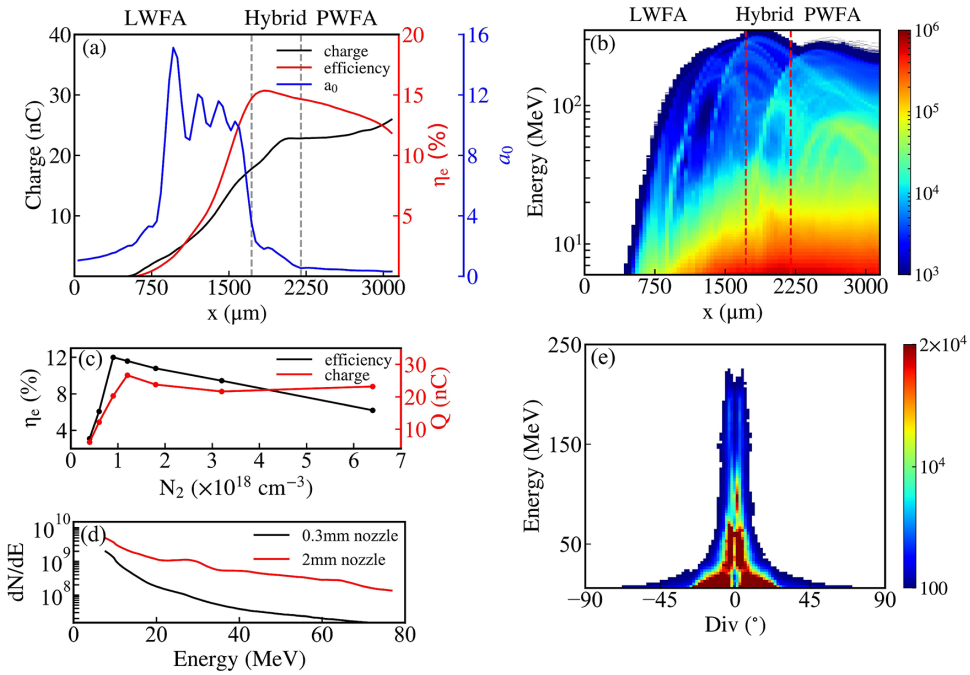


Figure 4. PIC simulation results for the 2-mm-diameter nozzle. (a) Temporal evolution of the laser intensity, total charge of electrons with energies of more than 6 MeV and the corresponding laser-to-electron energy conversion efficiency. (b) Evolution of the electron energy spectrum. (c) Laser-to-electron energy conversion efficiency and total electron charge as a function of nitrogen density. (d) Simulated energy spectra for the 0.3 and 2 mm nozzles. (e) Correlation between electron energy and divergence angle.

Figure 4(a) presents the evolution of the laser a_0, the total charge of electrons with energy above 6 MeV and the corresponding laser-to-electron energy conversion efficiency for the case of the 2 mm nozzle. The initial rapid rise in both energy conversion efficiency and electron charge is primarily due to the rapid transfer of energy from the laser to the plasma wakefield, which traps and accelerates a large number of electrons, yielding nearly 18 nC of charge. As the laser gradually depletes, the accelerated electron beam begins to drive the wakefield and transfers energy to multiple low-energy witness electron beams, sustaining continued charge growth, leading to a continued growth of charge up to approximately 26 nC. The conversion efficiency peaks at 15% for electrons above 6 MeV at $t \approx 6$ ps. Thereafter, as soon as a_0 drops, the LWFA–PWFA hybrid stage gradually transitions to pure PWFA, resulting in a decrease of the overall laser-to-electron efficiency. The electron energy spectrum evolution for the 2 mm nozzle is shown in Figure 4(b). During the LWFA stage, electrons are accelerated to the maximum energy of approximately 300 MeV by a highly nonlinear plasma wakefield. In the LWFA–PWFA hybrid and pure PWFA stages, the high-energy electron beam decelerates, while multiple electron beams are injected and accelerated to tens of MeV.

Figure 4(c) presents the dependence of laser-to-electron energy conversion efficiency and total electron charge on nitrogen plasma density for the 2 mm nozzle. For nitrogen densities below 0.9×10^{18} cm^{-3}, lower densities lead to slower laser energy depletion and stronger diffraction, resulting in inefficient energy transfer to electrons. At densities above 0.9×10^{18} cm^{-3}, higher densities cause faster laser depletion, prompting a rapid transition from the LWFA stage through the hybrid stage to the PWFA stage, leading to enhanced electron charge and conversion efficiency. However, rapid laser depletion prolongs the PWFA stage, ultimately causing a decline in both the average electron energy and conversion efficiency. Figure 4(d) compares the simulated energy spectra for the cases of the 0.3 and 2 mm nozzles. The case of the 2 mm nozzle yields a significantly stronger energy spectrum than the case of the 0.3 mm nozzle, in qualitative agreement with experimental observations. Notably, the energy spectrum of the 2 mm nozzle exhibits a distinct plateau around 30 MeV, closely matching the experimentally observed feature. However, the simulations predict more high-energy electrons than those experimentally observed for the 2 mm nozzle. This discrepancy may arise because higher-energy electrons, which typically exhibit smaller divergence angles (see Figure 4(e)), do not easily pass through the limited collimation aperture of the magnetic spectrometer.

5. Discussion

We compared the laser-to-electron energy conversion efficiencies achieved by different laser-driven acceleration mechanisms. In LWFA, the energy conversion efficiency from the laser to electrons is typically limited to a few

https://doi.org/10.1017/hpl.2025.10093 Published online by Cambridge University Press

percent[32–37], primarily because the total charge of electrons rarely exceeds several hundred pC. Even with self-truncated ionization injection, the electron charge typically reaches only the nC level[36]. Self-modulated LWFA can accelerate significantly higher charges than LWFA[38–41]. However, this mechanism relies on a picosecond and kJ-class laser facility, which is extremely rare around the world. DLA can generate electron beams with charges approaching 100 nC[42–47], but these beams typically exhibit relatively low energies and large divergences. Ponderomotive acceleration has demonstrated up to 14% conversion efficiency for electrons above 1.2 MeV, although the majority of the accelerated electrons remain below 10 MeV in energy[29]. In contrast, the self-mode transition from LWFA to PWFA offers a highly efficient acceleration mechanism that can significantly increase electron beam charge and enhance laser-to-electron energy conversion efficiency. The resulting tens of MeV electron beams with 100 nC charge, along with their secondary particles and radiations, are promising candidates for various applications. For example, they can efficiently pump nuclear isomers through photonuclear excitations[24,48] for studying short half-life nuclear energy levels, and generate short-pulsed high-flux neutrons via (γ, n) reaction[43] for industrial applications or nuclear data acquisition.

6. Conclusion

In summary, we have demonstrated a method for generating electron beams in the tens-of-MeV energy range with high laser-to-electron energy conversion efficiency. Through the comparison of 2 and 0.3 mm gas nozzles, gas density scans and simulations we find that the conversion efficiency is enhanced by the self-mode transition from LWFA to PWFA. The PIC simulations further confirm that the single-stage LPWFA mechanism helps deplete the laser energy and enables continual electron injection. The generated electron beams exhibit high charge, with measured charges of 31, 63 and 116 nC for electron energy above 6, 4 and 2 MeV, respectively. The corresponding laser-to-electron conversion efficiencies reach 6.1%, 10.7% and 16.4%, respectively, significantly exceeding those achieved in pure LWFA. The PIC simulations further confirm that the single-stage LPWFA mechanism depletes the laser energy and enables continual electron injection. These results clearly demonstrate that the single-stage LPWFA not only enhances energy conversion efficiency but also modulates the electron energy spectrum, significantly increasing the charge of tens-of-MeV electrons. This high-charge, tens-of-MeV, short-pulse electron beam enables efficient bremsstrahlung in high-Z converters, generating high-flux, short-pulse γ rays and producing photonuclear neutrons via the (γ, n) reaction. In addition, its broad electron spectrum, akin to space radiation conditions, makes it well suited for space radiation-hardness testing[49].

Acknowledgements

This work was supported by the National Natural Science Foundation of China (Grant Nos. 12335016, W2412039, 11991073 and 12305272) and the Strategic Priority Research Program of the Chinese Academy of Sciences (Grant Nos. XDA25030400, XDA25030800, XDA25010100 and XDA25010500). This work was carried out at the Synergetic Extreme Condition User Facility (SECUF, http://cstr.cn/31123.02.SECUF.D3). We thank Dr. Jun Zheng for helpful discussion.

Supplementary material

The supplementary material for this article can be found at http://doi.org/10.1017/hpl.2025.10093.

References

1. T. Tajima and J. M. Dawson, Phys. Rev. Lett. **43**, 267 (1979).
2. P. Chen, J. M. Dawson, R. W. Huff, and T. Katsouleas, Phys. Rev. Lett. **54**, 693 (1985).
3. B. Hidding, G. G. Manahan, O. Karger, A. Knetsch, G. Wittig, D. A. Jaroszynski, Z.-M. Sheng, Y. Xi, A. Deng, J. B. Rosenzweig, G. Andonian, A. Murokh, G. Pretzler, D. L. Bruhwiler, and J. Smith, J. Phys. B At. Mol. Phys. **47**, 234010 (2014).
4. B. Hidding, A. Beaton, L. Boulton, S. Corde, A. Doepp, F. Habib, T. Heinemann, A. Irman, S. Karsch, G. Kirwan, A. Knetsch, G. Manahan, A. Martinez De La Ossa, A. Nutter, P. Scherkl, U. Schramm, and D. Ullmann, Appl. Sci. **9**, 2626 (2019).
5. B. Hidding, R. Assmann, M. Bussmann, D. Campbell, Y.-Y. Chang, S. Corde, J. C. Cabadağ, A. Debus, A. Döpp, M. Gilljohann, J. Götzfried, F. M. Foerster, F. Haberstroh, F. Habib, T. Heinemann, D. Hollatz, A. Irman, M. Kaluza, S. Karsch, O. Kononenko, A. Knetsch, T. Kurz, S. Kuschel, A. Köhler, A. M. D. L. Ossa, A. Nutter, R. Pausch, G. Raj, U. Schramm, S. Schöbel, A. Seidel, K. Steiniger, P. Ufer, M. Yeung, O. Zarini, and M. Zepf, Photonics **10**, 99 (2023).
6. S. Gordienko and A. Pukhov, Phys. Plasmas **12**, 043109 (2005).
7. W. Lu, M. Tzoufras, C. Joshi, F. S. Tsung, W. B. Mori, J. Vieira, R. A. Fonseca, and L. O. Silva, Phys. Rev. Spec. Top. Accel. Beams **10**, 061301 (2007).
8. T. Kurz, T. Heinemann, M. F. Gilljohann, Y. Y. Chang, J. P. Couperus Cabadağ, A. Debus, O. Kononenko, R. Pausch, S. Schöbel, R. W. Assmann, M. Bussmann, H. Ding, J. Götzfried, A. Köhler, G. Raj, S. Schindler, K. Steiniger, O. Zarini, S. Corde, A. Döpp, B. Hidding, S. Karsch, U. Schramm, A. Martinez De La Ossa, and A. Irman, Nat. Commun. **12**, 2895 (2021).
9. F. M. Foerster, A. Döpp, F. Haberstroh, K. V. Grafenstein, D. Campbell, Y.-Y. Chang, S. Corde, J. P. Couperus Cabadağ, A. Debus, M. F. Gilljohann, A. F. Habib, T. Heinemann, B. Hidding, A. Irman, F. Irshad, A. Knetsch, O. Kononenko, A. Martinez De La Ossa, A. Nutter, R. Pausch, G. Schilling, A. Schletter, S. Schöbel, U. Schramm, E. Travac, P. Ufer, and S. Karsch, Phys. Rev. X **12**, 041016 (2022).

https://doi.org/10.1017/hpl.2025.10093 Published online by Cambridge University Press

10. S. Schöbel, R. Pausch, Y.-Y. Chang, S. Corde, J. Couperus Cabadağ, A. Debus, H. Ding, A. Döpp, F. M. Foerster, M. Gilljohann, F. Haberstroh, T. Heinemann, B. Hidding, S. Karsch, A. Köhler, O. Kononenko, T. Kurz, A. Nutter, K. Steiniger, P. Ufer, A. Martinez De La Ossa, U. Schramm, and A. Irman, New J. Phys. **24**, 083034 (2022).
11. B. Hidding, T. Königstein, J. Osterholz, S. Karsch, O. Willi, and G. Pretzler, Phys. Rev. Lett. **104**, 195002 (2010).
12. A. Martinez De La Ossa, R. W. Assmann, M. Bussmann, S. Corde, J. P. Couperus Cabadağ, A. Debus, A. Döpp, A. Ferran Pousa, M. F. Gilljohann, T. Heinemann, B. Hidding, A. Irman, S. Karsch, O. Kononenko, T. Kurz, J. Osterhoff, R. Pausch, S. Schöbel, and U. Schramm, Philos. Trans. R. Soc. A Math. Phys. Eng. Sci. **377**, 20180175 (2019).
13. J. P. Couperus Cabadağ, R. Pausch, S. Schöbel, M. Bussmann, Y.-Y. Chang, S. Corde, A. Debus, H. Ding, A. Döpp, F. M. Foerster, M. Gilljohann, F. Haberstroh, T. Heinemann, B. Hidding, S. Karsch, A. Koehler, O. Kononenko, A. Knetsch, T. Kurz, A. Martinez De La Ossa, A. Nutter, G. Raj, K. Steiniger, U. Schramm, P. Ufer, and A. Irman, Phys. Rev. Res. **3**, L042005 (2021).
14. K. H. Pae, I. W. Choi, and J. Lee, Phys. Plasmas **17**, 123104 (2010).
15. P. E. Masson-Laborde, M. Z. Mo, A. Ali, S. Fourmaux, P. Lassonde, J. C. Kieffer, W. Rozmus, D. Teychenné, and R. Fedosejevs, Phys. Plasmas **21**, 123113 (2014).
16. Y. Wu, C. Yu, Z. Qin, W. Wang, Z. Zhang, R. Qi, K. Feng, L. Ke, Y. Chen, C. Wang, X. Yang, Y. Leng, J. Liu, R. Li, and Z. Xu, Appl. Sci. **9**, 2561 (2019).
17. X. Chang, M. Zeng, J. Wang, and D. Li, New J. Phys. **27**, 023021 (2025).
18. V. Horný, P. G. Bleotu, D. Ursescu, V. Malka, and P. Tomassini, Phys. Rev. E **110**, 035202 (2024).
19. X. Zhang, V. N. Khudik, and G. Shvets, Phys. Rev. Lett. **114**, 184801 (2015).
20. T. Wang, V. Khudik, and G. Shvets, Phys. Rev. Accel. Beams **23**, 111304 (2020).
21. K. A. Tanaka, T. Yabuuchi, T. Sato, R. Kodama, Y. Kitagawa, T. Takahashi, T. Ikeda, Y. Honda, and S. Okuda, Rev. Sci. Instrum. **76**, 013507 (2005).
22. G. Boutoux, N. Rabhi, D. Batani, A. Binet, J.-E. Ducret, K. Jakubowska, J.-P. Nègre, C. Reverdin, and I. Thfoin, Rev. Sci. Instrum. **86**, 113304 (2015).
23. F. Ingenito, P. Andreoli, D. Batani, G. Boutoux, M. Cipriani, F. Consoli, G. Cristofari, A. Curcio, R. D. Angelis, G. D. Giorgio, J. Ducret, P. Forestier-Colleoni, S. Hulin, K. Jakubowska, and N. Rabhi, J. Instrum. **11**, C05012 (2016).
24. J. Feng, Y. Li, J. Tan, W. Wang, Y. Li, X. Zhang, Y. Meng, X. Ge, F. Liu, W. Yan, C. Fu, L. Chen, and J. Zhang, Laser Photonics Rev. **17**, 2300514 (2023).
25. A. Pukhov and J. Meyer-ter-Vehn, Appl. Phys. B Lasers Opt. **74**, 355 (2002).
26. J. L. Shaw, N. Lemos, L. D. Amorim, N. Vafaei-Najafabadi, K. A. Marsh, F. S. Tsung, W. B. Mori, and C. Joshi, Phys. Rev. Lett. **118**, 064801 (2017).
27. J. L. Shaw, N. Lemos, K. A. Marsh, D. H. Froula, and C. Joshi, Plasma Phys. Control. Fusion **60**, 044012 (2018).
28. R. Lehe, M. Kirchen, I. A. Andriyash, B. B. Godfrey, and J.-L. Vay, Comput. Phys. Commun. **203**, 66 (2016).
29. L. Martelli, O. Kononenko, I. A. Andriyash, J. Wheeler, J. Gautier, J.-P. Goddet, A. Tafzi, R. Lahaye, C. Giaccaglia, A. Flacco, V. Tomkus, M. Mackevičiūtė, J. Dudutis, V. Stankevic, P. Gečys, G. Račiukaitis, H. Kraft, X. Q. Dinh, and C. Thaury, Phys. Rev. Appl. **23**, 034033 (2025).
30. X. Yang, E. Brunetti, D. R. Gil, G. H. Welsh, F. Y. Li, S. Cipiccia, B. Ersfeld, D. W. Grant, P. A. Grant, M. R. Islam, M. P. Tooley, G. Vieux, S. M. Wiggins, Z. M. Sheng, and D. A. Jaroszynski, Sci. Rep. **7**, 43910 (2017).
31. J. Götzfried, A. Döpp, M. F. Gilljohann, F. M. Foerster, H. Ding, S. Schindler, G. Schilling, A. Buck, L. Veisz, and S. Karsch, Phys. Rev. X **10**, 041015 (2020).
32. S. P. D. Mangles, C. D. Murphy, Z. Najmudin, A. G. R. Thomas, J. L. Collier, A. E. Dangor, E. J. Divall, P. S. Foster, J. G. Gallacher, C. J. Hooker, D. A. Jaroszynski, A. J. Langley, W. B. Mori, P. A. Norreys, F. S. Tsung, R. Viskup, B. R. Walton, and K. Krushelnick, Nature **431**, 535 (2004).
33. C. G. R. Geddes, C. Toth, J. Van Tilborg, E. Esarey, C. B. Schroeder, D. Bruhwiler, C. Nieter, J. Cary, and W. P. Leemans, Nature **431**, 538 (2004).
34. J. Faure, Y. Glinec, A. Pukhov, S. Kiselev, S. Gordienko, E. Lefebvre, J.-P. Rousseau, F. Burgy, and V. Malka, Nature **431**, 541 (2004).
35. H. T. Kim, K. H. Pae, H. J. Cha, I. J. Kim, T. J. Yu, J. H. Sung, S. K. Lee, T. M. Jeong, and J. Lee, Phys. Rev. Lett. **111**, 165002 (2013).
36. J. P. Couperus, R. Pausch, A. Köhler, O. Zarini, J. M. Krämer, M. Garten, A. Huebl, R. Gebhardt, U. Helbig, S. Bock, K. Zeil, A. Debus, M. Bussmann, U. Schramm, and A. Irman, Nat. Commun. **8**, 487 (2017).
37. L. T. Ke, K. Feng, W. T. Wang, Z. Y. Qin, C. H. Yu, Y. Wu, Y. Chen, R. Qi, Z. J. Zhang, Y. Xu, X. J. Yang, Y. X. Leng, J. S. Liu, R. X. Li, and Z. Z. Xu, Phys. Rev. Lett. **126**, 214801 (2021).
38. M. I. K. Santala, Z. Najmudin, E. L. Clark, M. Tatarakis, K. Krushelnick, A. E. Dangor, V. Malka, J. Faure, R. Allott, and R. J. Clarke, Phys. Rev. Lett. **86**, 1227 (2001).
39. F. Albert, N. Lemos, J. L. Shaw, P. M. King, B. B. Pollock, C. Goyon, W. Schumaker, A. M. Saunders, K. A. Marsh, A. Pak, J. E. Ralph, J. L. Martins, L. D. Amorim, R. W. Falcone, S. H. Glenzer, J. D. Moody, and C. Joshi, Nucl. Fusion **59**, 032003 (2019).
40. N. Lemos, F. Albert, J. L. Shaw, D. Papp, R. Polanek, P. King, A. L. Milder, K. A. Marsh, A. Pak, B. B. Pollock, B. M. Hegelich, J. D. Moody, J. Park, R. Tommasini, G. J. Williams, H. Chen, and C. Joshi, Plasma Phys. Control. Fusion **60**, 054008 (2018).
41. J. L. Shaw, M. A. Romo-Gonzalez, N. Lemos, P. M. King, G. Bruhaug, K. G. Miller, C. Dorrer, B. Kruschwitz, L. Waxer, G. J. Williams, M. V. Ambat, M. M. McKie, M. D. Sinclair, W. B. Mori, C. Joshi, H. Chen, J. P. Palastro, F. Albert, and D. H. Froula, Sci. Rep. **11**, 7498 (2021).
42. C. Gahn, G. D. Tsakiris, A. Pukhov, J. Meyer-ter-Vehn, G. Pretzler, P. Thirolf, D. Habs, and K. J. Witte, Phys. Rev. Lett. **83**, 4772 (1999).
43. I. Pomerantz, E. McCary, A. R. Meadows, A. Arefiev, A. C. Bernstein, C. Chester, J. Cortez, M. E. Donovan, G. Dyer, E. W. Gaul, D. Hamilton, D. Kuk, A. C. Lestrade, C. Wang, T. Ditmire, and B. M. Hegelich, Phys. Rev. Lett. **113**, 184801 (2014).
44. M. M. Günther, O. N. Rosmej, P. Tavana, M. Gyrdymov, A. Skobliakov, A. Kantsyrev, S. Zähter, N. G. Borisenko, A. Pukhov, and N. E. Andreev, Nat. Commun. **13**, 170 (2022).
45. O. N. Rosmej, M. Gyrdymov, M. M. Günther, N. E. Andreev, P. Tavana, P. Neumayer, S. Zähter, N. Zahn, V. S. Popov, N. G. Borisenko, A. Kantsyrev, A. Skobliakov, V. Panyushkin, A. Bogdanov, F. Consoli, X. F. Shen, and A. Pukhov, Plasma Phys. Control. Fusion **62**, 115024 (2020).
46. P. Tavana, N. Bukharskii, M. Gyrdymov, U. Spillmann, Ş. Zähter, J. Cikhardt, N. G. Borisenko, P. Korneev, J. Jacoby, C. Spielmann, N. E. Andreev, M. M. Günther, and O. N. Rosmej, Front. Phys. **11**, 1178967 (2023).
47. M. Gyrdymov, J. Cikhardt, P. Tavana, N. G. Borisenko, S. Y. Gus´kov, R. A. Yakhin, G. A. Vegunova, W. Wei, J. Ren,

https://doi.org/10.1017/hpl.2025.10093 Published online by Cambridge University Press

Y. Zhao, D. H. H. Hoffmann, Z. Deng, W. Zhou, R. Cheng, J. Yang, J. Novotny, X. Shen, A. Pukhov, J. Jacoby, C. Spielmann, V. S. Popov, M. E. Veysman, N. E. Andreev, and O. N. Rosmej, Sci. Rep. **14**, 14785 (2024).
48. P. Walker and G. Dracoulis, Nature **399**, 35 (1999).
49. B. Hidding, O. Karger, T. Königstein, G. Pretzler, G. G. Manahan, P. McKenna, R. Gray, R. Wilson, S. M. Wiggins, G. H. Welsh, A. Beaton, P. Delinikolas, D. A. Jaroszynski, J. B. Rosenzweig, A. Karmakar, V. Ferlet-Cavrois, A. Costantino, M. Muschitiello, and E. Daly, Sci. Rep. **7**, 42354 (2017).

https://doi.org/10.1017/hpl.2025.10093 Published online by Cambridge University Press